Simplify your imaging workflows

Make research imaging workflows accessible, traceable, and secure with Athena Software for Core Imaging Facilities.

Thermo Scientific™ Athena Software is a premium imaging data management platform designed for core imaging facilities that support materials science research.

Athena Software ensures traceability of images, metadata, and experimental workflows through an intuitive and collaborative web interface.

Find out more at **thermofisher.com/athena**

ThermoFisher SCIENTIFIC

ADVANCED OPTICAL MATERIALS
www.advopticalmat.de

Van der Waals $PdSe_2/WS_2$ Heterostructures for Robust High-Performance Broadband Photodetection from Visible to Infrared Optical Communication Band

*Xiaolin Kang, Changyong Lan, Fangzhou Li, Wei Wang, SenPo Yip, You Meng, Fei Wang, Zhengxun Lai, Chuntai Liu, and Johnny C Ho**

Due to excellent electrical and optoelectronic properties, 2D transition metal dichalcogenides and their van der Waals (vdW) heterostructures have attracted great attention for broadband optoelectronics. Here, an unreported vdW $PdSe_2/WS_2$ heterostructure is developed for robust high-performance broadband photodetection from visible to infrared optical communication band. These heterostructure devices are simply formed by direct selenization of Pd films pre-deposited on the chemical vapor deposited monolayer WS_2, followed by wet-transfer onto device substrates with pre-patterned electrodes. Importantly, the obtained heterostructure device exhibits an impressive broadband spectral photoresponse with response times less than 100 ms for different wavelength regions (532 to 1550 nm), where this performance is significantly better than that of pristine monolayer WS_2 devices. This performance enhancement is attributed to the type I band alignment of the heterostructure. Under illumination, both intralayer and interlayer excitations are involved to generate carriers in the relevant layer, enabling the broadband photoresponse. Photocarriers would then undergo charge separation in the depletion region with electrons transferred into the charge transport layer of WS_2 through the built-in electric field, followed by the relaxation to valance band via interlayer or intralayer transition. All these findings can indicate the promising potential of vdW $PdSe_2/WS_2$ heterostructures for next-generation high-performance optoelectronics.

1. Introduction

In recent years, because of the extraordinary physical and electrical properties, 2D transition metal dichalcogenides (TMDs) have attracted tremendous interest as the active device materials for electronics and optoelectronics;[1] however, their relatively large intrinsic band gap (>1 eV) has inevitably restricted the utilization for photodetectors in the infrared optical communication band and beyond.[1d,2] In order to widen the spectral range and to enhance the photoresponse of TMDs, van der Waals (vdW) heterostructures with two different TMDs materials have been extensively explored to take advantages of not only the improved light absorption but also the interlayer interaction of both materials under light illumination.[3] It has been shown that 2D vdW TMDs heterostructures tend to exhibit strong light–matter interaction due to their appropriate band alignment when the TMDs layers are stacked in contact with each other, extending the spectral response.[3d,4] More importantly, these heterointerfaces can also separate the photo-excited charge carriers more efficiently for the existence of built-in electric field, leading to improved photodetection performance.[3a,d,5] Generally, there are two major approaches to fabricate 2D vdW TMDs heterostructures: physical stacking method[5c,6] and two-step chemical vapor deposition (CVD) method.[3d,e,7] For physical stacking, although the exfoliated TMDs preserve the high material quality, the subsequent stacking process would usually introduce interfacial contamination that deteriorates the fabricated device performance.[8] Besides, the stacking procedures

X. Kang, Dr. F. Li, W. Wang, Dr. S. P. Yip, Y. Meng, Dr. F. Wang, Z. Lai, Prof. J. C. Ho
Department of Materials Science and Engineering
City University of Hong Kong
Hong Kong 999 077, China
E-mail: johnnyho@cityu.edu.hk

Dr. C. Lan
State Key Laboratory of Electronic Thin Films and Integrated Devices
University of Electronic Science and Technology of China
Chengdu 610 054, China

The ORCID identification number(s) for the author(s) of this article can be found under https://doi.org/10.1002/adom.202001991.

DOI: 10.1002/adom.202001991

Dr. S. P. Yip, Dr. F. Wang, Prof. J. C. Ho
State Key Laboratory of Terahertz and Millimeter Waves
City University of Hong Kong
Hong Kong 999 077, China

Dr. C. Liu
Key Laboratory of Advanced Materials Processing & Mold (Zhengzhou University)
Ministry of Education
Zhengzhou 450 002, China

Prof. J. C. Ho
Institute for Materials Chemistry and Engineering
Kyushu University
Fukuoka 816-8580, Japan

are not suitable for large-scale device manufacturing. In CVD processes, the successive TMDs growth is capable to produce high-quality heterostructures with excellent electrical and optoelectronic functionalities, while it remains challenging to generalize a universal route to achieve different stacking configurations on a large scale applicable for most vdW TMDs heterostructures.[3e,6a,c,9] At the same time, direct sulfurization or selenization of transitional metal thin films can as well be utilized in a simple manner to synthesize large-area TMDs with well-controlled thickness and uniformity despite the polycrystalline structure.[4,10]

Among many 2D TMDs semiconductors, monolayer WS_2 has been widely studied owing to its high carrier mobility, excellent photoluminescence (PL) emission efficiency, and thus superior quantum efficiency.[1b,2a,11] When monolayer WS_2 is decorated with other semiconductor materials, the type-II band alignment can be established to further enhance the optoelectronic performance of heterostructure devices.[12] For example, in our previous work, the WS_2/CdS heterostructure exhibit better photodetection under 450 nm excitation, as compared to the pristine WS_2 structure, since photo-excited electrons would get transferred effectively from CdS into WS_2 through the heterointerface.[12a] For the hybrid WS_2/perovskite (PVK) material system, the improved interfacial charge carrier separation could lead to pronounced photodetection, including fast photoresponse speed and high responsivity.[12b,c] Moreover, Pan et al. reported that the ultrathin PVK/WS_2 vertical heterostructure could achieve outstanding optoelectronics characteristics with the optimal response time down to 64 μs and the responsivity up to 11 174.2 A/W towards 520 nm illumination wavelength. Lately, 2D palladium diselenide ($PdSe_2$) has become an emerging semiconductor for wide spectral photodetection.[4,13] It has a broad tunable band gap ranging from 0 eV for bulk all the way up to 1.3 eV for monolayers, with high carrier mobility reaching 4×10^4 cm^2 V^{-1} s^{-1} and better air stability.[13b,14] In fact, $PdSe_2$ nanocrystals obtained by mechanical exfoliation or vapor-phase methods would exhibit *p*-type, *n*-type, or ambipolar transport behaviors heavily depending on the material synthesis conditions.[13–15] Attributed to all the above unique properties, vdW *p*–*n* heterojunctions based on $PdSe_2$ have shown the promising and exceptional electronic and optoelectronic performance.[3d,4,16] To be specific, *p*-BP/*n*-$PdSe_2$ photodiodes were realized to have tunable and high rectification up to 7.1×10^5 as well as high photoresponsivity and detectivity in visible and infrared regions, but the ambient stability of BP materials is still questionable.[16] Without using BP materials, *p*-GeSe/*n*-$PdSe_2$ heterojunction diodes could serve as a good platform for photodetection with high external quantum efficiency and large rectification behaviors for the visible light region.[17]

Apart from the selection of TMDs materials, the proper design of heterostructures to involve both photosensing and charge conduction channels has also been actively investigated with the aim to maximize the effective device area for photodetection, further elevating the photodetector performance.[6a,12b,16,18] In particular, Shin et al. fabricated the WSe_2/MoS_2 vdW heterostructure with ultrasensitive photodetection performance under 532 nm laser illumination, where MoS_2 served as the conduction channel with photogenerated electrons collected and transferred from WSe_2 into MoS_2 via the built-in electric field.[18a] The non-photodiode-based PVK/graphene heterostructure was also reported for the efficient photo-excited electron–hole pair separation, contributing to the enhanced photogain, response speed, and high responsivity of ≈10^5 A W^{-1} in the visible wavelength region.[19] Nevertheless, there are still limited studies concentrating on the reliable broadband photodetection using the optimal vdW heterostructure. Here, we develop an unreported vdW $PdSe_2/WS_2$ heterostructure for the robust high-performance broadband photodetection from visible to infrared optical communication band. It is noteworthy that the heterostructure is simply formed by the direct selenization of Pd films pre-deposited on the CVD-grown monolayer WS_2. The obtained vdW $PdSe_2/WS_2$ heterostructure is then wet-transferred onto the device substrate with pre-patterned Au/Ti source/drain electrodes. In this case, the entire top $PdSe_2$ film is a photosensitive layer due to its strong absorption over a wide spectral range together with the bottom monolayer WS_2 serving as the charge transfer interface. Because of the built-in electrical field in the vicinity of heterointerface, there would not be any interlayer charge transfer during carrier transport and collection. As a result, the vdW $PdSe_2/WS_2$ heterostructure exhibits a strong photoresponse from 532 to 1550 nm light illumination with efficient response times less than 100 ms for different wavelength regions, where this performance is significantly better than that of pristine monolayer WS_2 devices. All these results can evidently indicate the promising potential of vdW $PdSe_2/WS_2$ heterostructures for reliable high-performance optoelectronics.

2. Results and Discussion

Figure 1a presents the schematic illustration of the fabrication process of vdW $PdSe_2/WS_2$ heterostructure devices, where the monolayer WS_2 is initially synthesized via the CVD method followed by the subsequent Pd deposition, selenization, and final transfer of the entire as-grown heterostructure film onto the device substrate pre-deposited with electrode patterns. In order to characterize the morphology of obtained films, atomic force microscopy is conducted to determine the thickness of $PdSe_2/WS_2$ and pristine $PdSe_2$ films, which are found to be 4.04 and 3.30 nm, respectively, based on their height profiles (Figure 1b). The height difference is 0.74 nm that is perfectly consistent with the thickness of monolayer WS_2.[11c] The feasibility of seleniztion is confirmed by the X-ray photoelectron spectroscopy (XPS) measurement of $PdSe_2$, where the binding energies of Pd $3d_{3/2}$ (342.1 eV), Pd $3d_{5/2}$ (336.8 eV), Se $3d_{3/2}$ (55.6 eV), and Se $3d_{5/2}$(54.8 eV) shown in Figure S1, Supporting Information, are consistent with the characteristic binding energies of $PdSe_2$ crystals.[14] It should also be noticed that the $PdSe_2$ film over-grown on the monolayer WS_2 has the smoother surface than that directly grown on SiO_2/Si substrates, which can be attributed to the atomic flatness of the underlying monolayer WS_2. It is remarkable to obtain the smooth $PbSe_2$ film for high-quality vdW $PdSe_2/WS_2$ heterostructures by using the simple selenization process here, in which the relatively easy fabrication procedures for vdW heterostructures would be advantageous for large-scale device construction.

Moreover, the uniformity and structural properties of $PdSe_2/WS_2$, $PdSe_2$, and WS_2 films are examined by additional

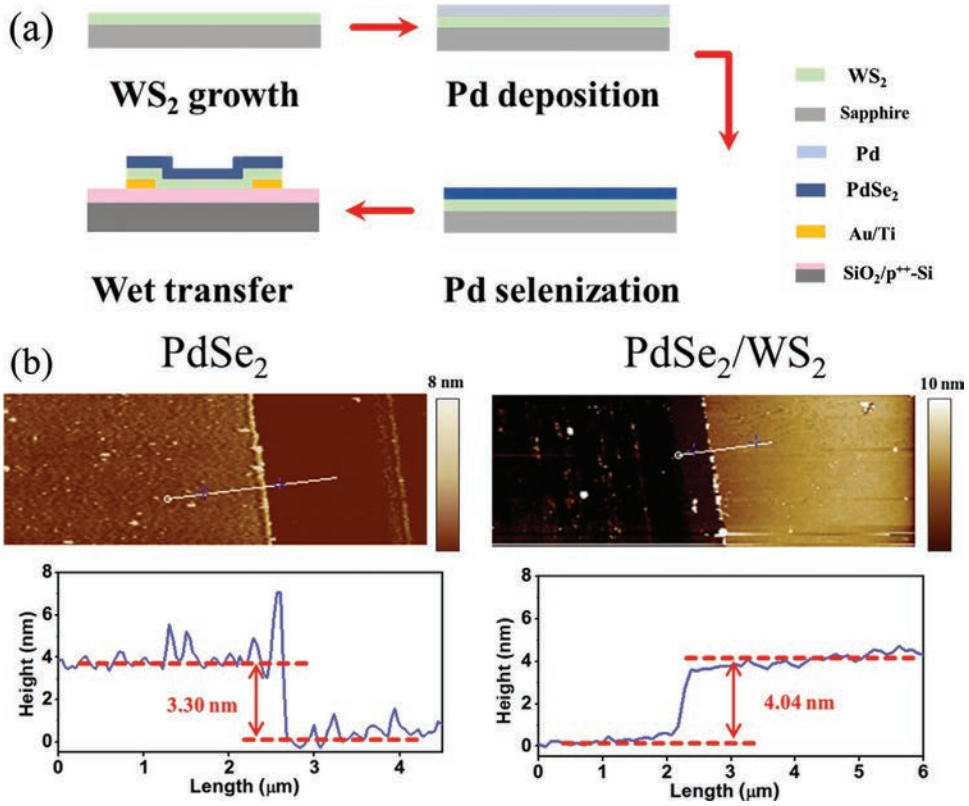

Figure 1. Device fabrication and atomic force microscopy characterization. a) Schematic illustration of the synthesis of vdW $PdSe_2/WS_2$ heterostructure and fabrication of the corresponding device. b) Atomic force microscope images and corresponding height profiles of $PdSe_2$ and $PdSe_2/WS_2$ films, respectively.

characterization techniques. As shown in **Figure 2**a, different regions on the partial overlap of vdW $PdSe_2/WS_2$ heterostructure are measured by Raman spectroscopy, with the regions identified and enclosed by blue and orange dashed lines. It is observed that the spatially-resolved Raman mapping result is well correlated with Raman peaks at both 352 (Figure 2b) and 256 cm^{-1} (Figure 2c), which correspond to the characteristic E^1_{2g} mode of WS_2 and A^3_g mode of $PdSe_2$, respectively.[11c,15b] Both mapping results reveal a homogeneous and distinctive contrast, indicating the formation of the uniform vdW $WS_2/PdSe_2$ heterostructure in this work. Besides, Figure 2d illustrates the extracted Raman spectra at three different regions. It is clear that there are two characteristic peaks corresponding to E^1_{2g} (352 cm^{-1}) and A_{1g} modes (419 cm^{-1}) for the spectrum of monolayer WS_2,[2a,11c] while there are two distinctive peaks associating with the A^1_g-B^1_g (143 cm^{-1}) and A^3_g (256 cm^{-1}) modes for the spectrum of $PdSe_2$ film.[4,13a] When it comes to Raman spectrum of $PdSe_2/WS_2$ heterostructure film, all the characteristic peaks assigned to both constituents are evidently observed. In Figure 2b,d, the Raman peak intensity of E^1_{2g} mode in the $PdSe_2/WS_2$ stacking region is a bit smaller than that in pure WS_2 region, which is attributed to the partial absorption of the excitation power and the Raman signals by the overgrown $PdSe_2$ film. It can also be inferred that the selenization process at 420 °C does not induce any damage to the underlying monolayer WS_2 monolayer since there are not any significant changes to the Raman peak positions of WS_2 observed for the direct exposure to the selenization process. In order to further confirm this point, XPS is performed on the pristine monolayer WS_2 and the WS_2 that experienced seleniztion process to assess their chemical composition and valence states. As depicted in Figure 2e, there are characteristic peaks related to W $5p_{3/2}$, W $4f_{5/2}$, and W $4f_{7/2}$ for both samples observed, where no distinctive shift among those peaks corresponding to the same orbital occurs. The W-O peak indicates the partial oxidation of the WS_2 film that can be ascribed to the photo-induced process in ambient.[21] Regarding the S species in WS_2 exposed to the selenization condition, peaks associated with S $2p_{1/2}$ and S $2p_{3/2}$ are displayed in Figure 2f (bottom) and found in common with the characteristic S-2p peaks (top) of the pristine monolayer WS_2 without any evidence of the Se-3s/3p orbitals. Furthermore, the XPS spectrum of monolayer WS_2 experienced with the selenization process did not show any peaks of Se-3d orbitals (Figure 2g),[22] which is consistent with the observations described above. These results can obviously indicate that the employed selenization process is moderate and confirmed again not to alter the chemical composition of WS_2. More importantly, transmission electron microscopy (TEM) is further performed to investigate the crystallinity of monolayer WS_2 and $PdSe_2$ films. Samples for TEM measurement were transferred onto the TEM grids via polymer-assisted wet-transfer method.[11a,12a,20] Figure 2h,i present the high-resolution TEM images of $PdSe_2$ film and monolayer WS_2, respectively. It is seen that the $PdSe_2$ film is polycrystalline,

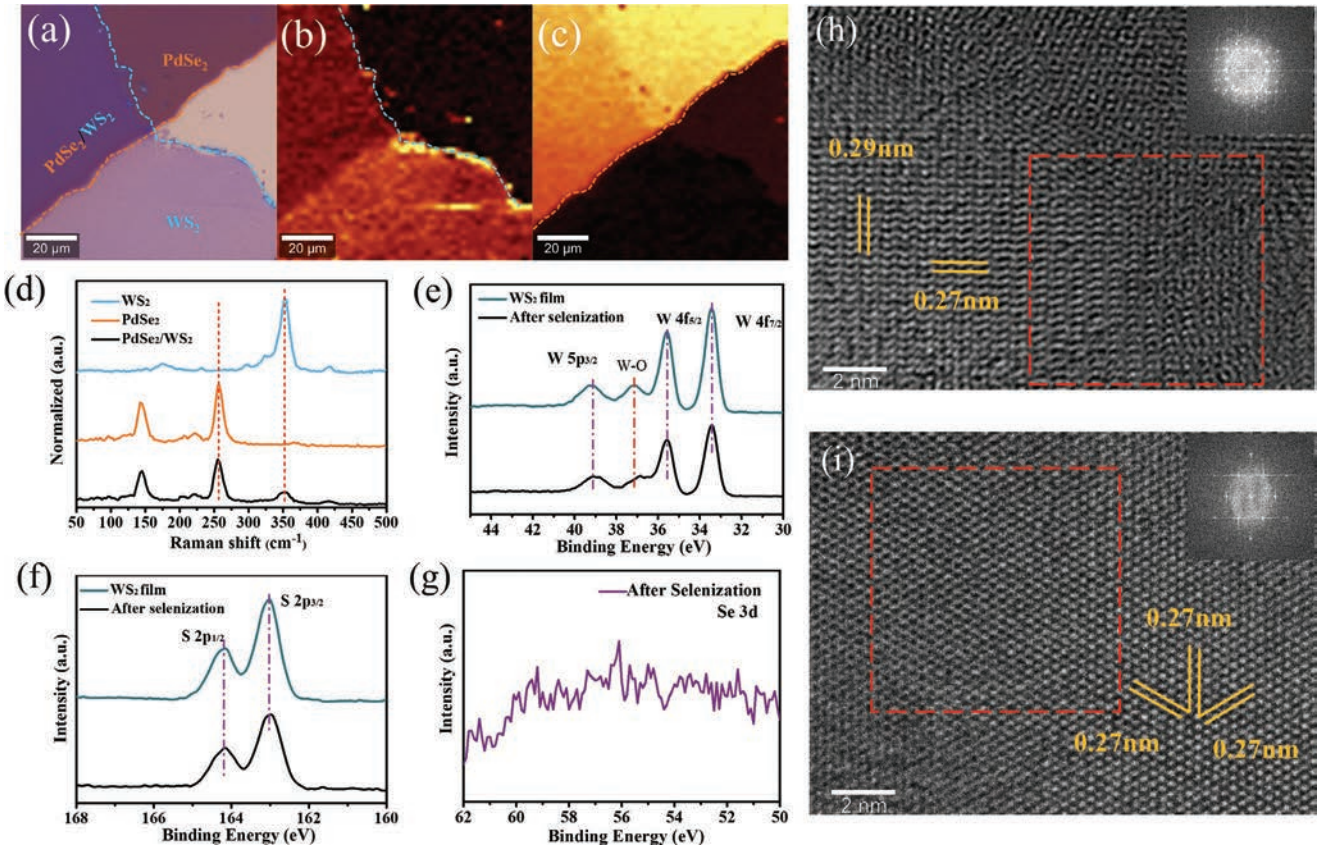

Figure 2. Characterization of $PdSe_2/WS_2$, WS_2 and $PdSe_2$ films. a) Optical image of the partially stacked $PdSe_2/WS_2$ film. b,c) Raman mapping of the stacked film excited at 532 nm, correlated with E_{2g} mode of the monolayer WS_2 collected at 352 cm^{-1}(b) and A_g mode of $PdeSe_2$ collected at 256 cm^{-1} (c), respectively. d) Raman spectra of the stacked film extracted from the regions corresponding to WS_2, $PdSe_2$, and $PdSe_2/WS_2$, respectively. e) XPS spectra of W 4f peak. f) XPS spectra of S 2p peak. g) XPS spectra of Se 3d peak. h,i) High-resolution transmission electron microscope image of $PdSe_2$ (h) and WS_2 (i) films. Insets show the corresponding FFT pattern of selected regions.

of which the fast Fourier transformation (FFT) image exhibits the stacking of multiple sets of diffraction patterns at different orientations (Figure 2h inset).[15b] On the other hand, the monolayer WS_2 is highly crystalline with identified lattice spacing of 0.27 nm, which is ascribed to (110) planes of WS_2 together with the FFT result further confirming its hexagonal crystal structure (Figure 2i inset).[11c,12a] All these findings can clearly demonstrate the successful fabrication of high-quality vdW heterostructure with polycrystalline $PdSe_2$ stacking on top of monolayer WS_2, being essential for subsequent device studies.

In addition, it is also important to evaluate the optical properties of $PdSe_2/WS_2$, $PdSe_2$, and WS_2 films for the development of photodetectors. **Figure 3**a shows the optical absorption spectra of all the prepared films. There are two distinctive peaks positioned at 514 and 611 nm for the pristine monolayer WS_2, where they are associated with the excitonic absorptions of the direct gap located at K valley of the Brillouin zone. The separation of these two peaks stems from the splitting of valance band minimum (VBM) due to the spin-orbit coupling at K valley, which is found almost constant and regardless of the film thickness.[12c,23] As for $PdSe_2$, it is pronounced that $PdSe_2$ displays the higher absorbance than monolayer WS_2 over the detection range owing to its larger thickness. When it comes to the optical absorption of $PdSe_2/WS_2$ heterostructure, its absorbance is the highest with the visibility of characteristic peaks of the underlying monolayer WS_2. In this case, the $PdSe_2/WS_2$ heterostructure can achieve the enhanced light absorption in order to facilitate light-matter interactions for high-performance photodetection. Simultaneously, PL spectra of $PdSe_2/WS_2$ and WS_2 are as well collected at a laser excitation of 532 nm in order to further investigate their photophysical properties. As depicted in Figure 3b, monolayer WS_2 exhibits the strong PL emission with the dominant emission peak at 1.99 eV, corresponding to the recombination of excitons.[5d,12c] However, the $PdSe_2/WS_2$ heterostructure gives the evident PL quenching and a rather weak PL emission, which indicates that the strong charge carrier transfer takes place between $PdSe_2$ and WS_2.[3d,e,24] As a result, under light illumination, the photoexcited electrons and holes in WS_2 are inclined to transfer into low-energy states in $PdSe_2$ rather than existing as excitons due to the type I heterostructure (see the band alignment in Figure 3c), which thus lead to the significant PL quenching of the $PdSe_2/WS_2$ heterostructure. To further understand this charge transfer process, PL spectra were deconvoluted to reveal the different contribution from exciton (X) and trion (X^-). As shown in Figure S2a,b, Supporting Information, there is not any shift of the X peaks while a blue-shift observed for the X^- peak in the $PdSe_2/WS_2$ heterostructure as compared with that

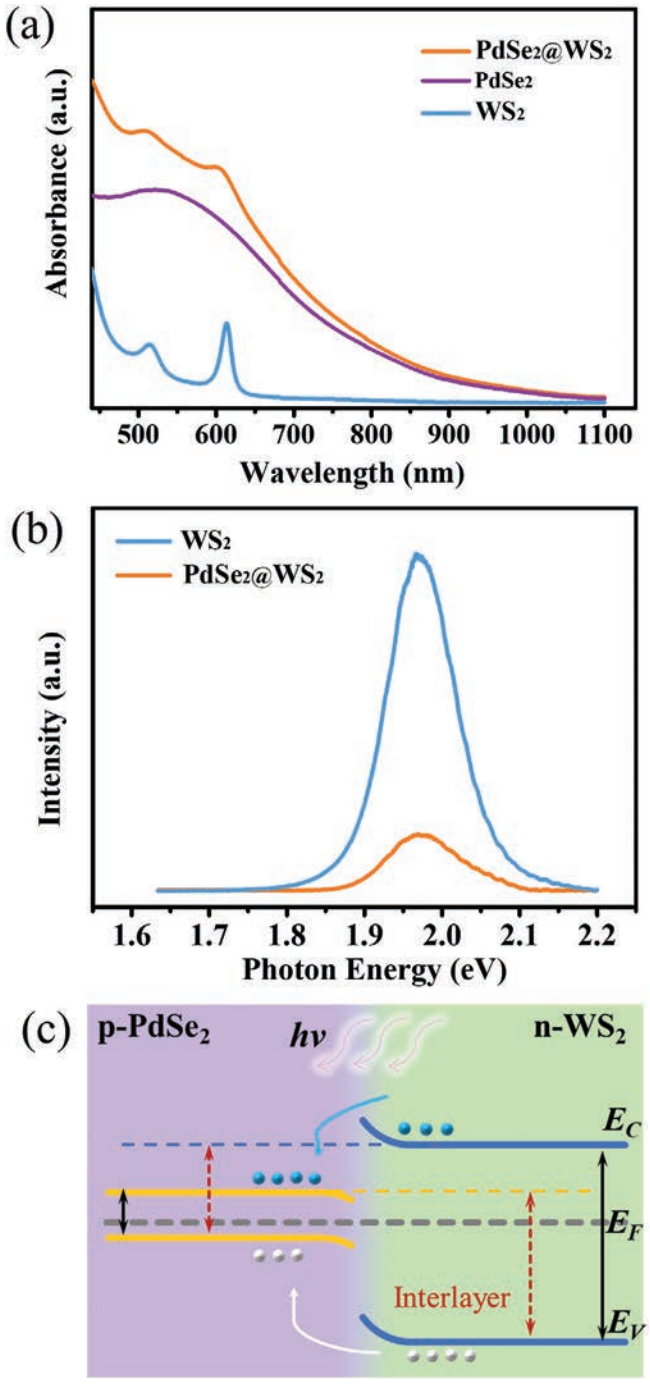

Figure 3. Optical properties of the vdW $PdSe_2/WS_2$ heterostructure. a) Ultraviolet–visible–near infrared absorption spectra of the monolayer WS_2, $PdSe_2$, and $PdSe_2/WS_2$ heterostructure. b) PL spectra of monolayer WS_2 and $PdSe_2/WS_2$ heterostructure. c) Energy band alignment diagram of vdW *p–n* $PdSe_2/WS_2$ heterojunction. E_F, E_V, and E_C stand for Fermi level, valence band, and conduction band, respectively.

in WS_2, suggesting the reduced electron density of WS_2 in the heterostructure.[25] These observations can confirm the charge transfer process as described in Figure 3c, which provides valuable information to understand the improved performance of $PdSe_2/WS_2$ heterostructure photodetectors in the later section.

To shed light on the electrical transport properties of individual monolayer WS_2 and polycrystalline $PdSe_2$ films, field-effect transistors (FETs) were fabricated by transferring these films onto SiO_2 (270 nm)/p^{++}-Si substrates, where Au/Ti source/drain electrodes had been pre-patterned on the surface. In detail, the $PdSe_2$ FET exhibits the obvious *p*-type transport behaviors with a large hysteresis in ambient with an on/off current ratio of about 10^3 (Figure S3a, Supporting Information), whereas it changes to give the ambipolar transport characteristics with both on/off current ratio (i.e., *p*-type and *n*-type conductivity) less than 10^2 in vacuum (Figure S3b, Supporting Information). The carrier mobility is then calculated based on the analytical equation of

$$\mu = \frac{L}{W} \times \frac{dI_{ds}}{dV_{gs}} \times \frac{1}{C_{ox}V_{ds}} \quad (1)$$

where L and W are the channel length (2 μm) and width (220 μm), respectively, C_{ox} is the capacitance per unit area (1.27×10^{-4} F m^{-2}) and V_{ds} is 0.1 V. For the reverse gate voltage sweeping, the maximum hole mobility of $PdSe_2$ FET is about 1.16×10^{-2} cm^2 V^{-1} s^{-1} measured in ambient, while the maximum hole and electron mobility are both close to 5.8×10^{-4} cm^2 V^{-1} s^{-1} assessed in vacuum. As the adsorbates, such as H_2O and O_2, located on the surface of $PdSe_2$ can accept electrons from $PdSe_2$, leading to *p*-doping; therefore, the hole carrier density is expected to be higher in ambient than that in vacuum.[26] This way, the charge trapping would become less efficient under the high hole density, contributing to the increased carrier mobility in ambient.

After that, the electrical charge transport properties and optoelectronic performance of the vdW $PdSe_2/WS_2$ heterostructure FET are evaluated. **Figure 4**a (top) depicts the schematic illustration of the back-gate device configuration while the optical image (bottom) shows the top-view of the fabricated device. As given in the transfer characteristics in Figure 4b, the vdW $PdSe_2/WS_2$ heterostructure device shows the *p*-type dominated ambipolar behaviors in ambient under dark, indicating that the holes dominate charge transport process is witnessed under the negative gate bias. The corresponding output characteristics present the linear relationship of I_{ds}–V_{ds} curves at both negative and positive gate bias (Figure 4c), revealing the ohmic-like contact between channel materials and metal electrodes. Evidently, I_{ds} decreases with the gate voltage varying from –80 to –20 V while I_{ds} experiences an increasing trend as the gate bias changes from 0 to 80 V. The calculated hole and electron mobility values under reverse gate voltage sweeping at $V_{ds} = 0.1$ V are found to be 3.5×10^{-2} and 2.7×10^{-4} cm^2 V^{-1} s^{-1}, respectively. Nevertheless, it is the monolayer WS_2 rather than the $PdSe_2$ layer that is designed in contact with source/drain electrodes in our device configuration. Charge carriers in $PdSe_2$ can easily tunnel into electrodes due to the ultrathin thickness of the monolayer WS_2. Although the monolayer WS_2 is an *n*-type semiconductor with a large conductivity under positive gate bias in vacuum (Figure S4, Supporting Information), its counterpart in the heterostructure shows the much lower electrical conductivity at the same gate bias which can be inferred from the slope of output characteristics in Figure S5a, Supporting Information. The possible physical picture for the

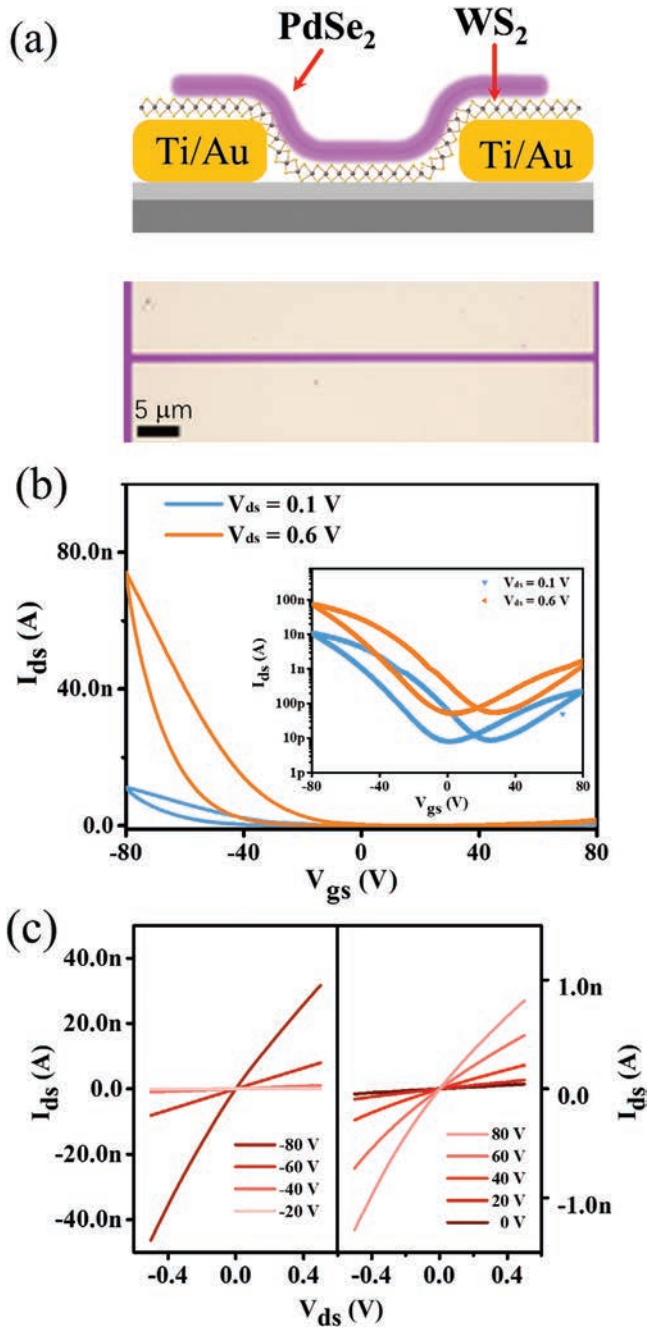

Figure 4. Electrical properties of the vdW $PdSe_2/WS_2$ heterostructure device. a) Top panel: Schematic image of the $PdSe_2/WS_2$ transistor. Bottom panel: top-view optical image of the $PdSe_2/WS_2$ device. b)Transfer characteristics of the $PdSe_2/WS_2$ device, V_{ds} = 0.1 and 0.6 V. Inset shows the transfer curves in a semi-log scale. c) Output characteristics of the $PdSe_2/WS_2$ device under different V_{gs}.

above transport behaviors of the heterostructure in vacuum might come from the gate bias induced electrons in WS_2 that are transferred to the $PdSe_2$ side due to type I heterostructure. That means that the electrons in WS_2 are depleted. Since $PdSe_2$ has a very low electron carrier mobility as compared with that in WS_2, this would lead to the low output current under positive gate bias in comparison with the pure WS_2 FET. On the contrary, the vdW $PdSe_2/WS_2$ heterostructure exhibits the *n*-type dominated ambipolar transport behaviors once the device is operated in vacuum (Figure S5b, Supporting Information). Also, its corresponding conductivity is much higher than that of $PdSe_2$ film alone under the same condition (Figure S3b, Supporting Information), which implies the decent contribution from WS_2 to the entire conductance of the $PdSe_2/WS_2$ heterostructure at positive gate bias. At the same time, devices of $PdSe_2/WS_2$ heterojunction sandwiched between source/drain electrodes along the vertical direction are as well fabricated as shown in Figure S6a, Supporting Information, (top: device schematic illustration; bottom: corresponding top-view optical image). It is anticipated that the I_{ds}–V_{ds} curve shows a clear current-rectifying behavior (Figure S6b, Supporting Information), which is consistent with traditional diode characteristics. This result would demonstrate the successful formation of *p*–*n* junction here and confirm the built-in electrical field established in the vdW $PdSe_2/WS_2$ heterostructure. The influence of adsorbates can be further revealed by comparing the output curves of $PdSe_2$ (Figure S3c,d, Supporting Information) or $PdSe_2/WS_2$ (Figure 4c and Figure S5a, Supporting Information) heterostructure devices measured in ambient and those measured in vacuum. Apparently, the conductivity of $PdSe_2$ in ambient is much larger than that in vacuum, which indicates the distinct *p*-doping of adsorbates. Similarly, the *n*-type transport of WS_2 is suppressed by the *p*-doping effect of adsorbates. Since the thickness of the $PdSe_2$ top layer is smaller than the Debye screening length, the adsorbates could also influence the carrier concentration of the bottom WS_2 layer.[26c]

For photodetector performance, the photoresponse properties of the vdW $PdSe_2/WS_2$ heterostructure are first carefully examined. It is widely known that the efficient separation of photoexcited electron–hole pairs would occur under light illumination for the existence of built-in electric field at the interface of the het erostructure.[3b,e,9] Even though our device does not have the conventional configuration of *p*–*n* diodes, there is still a built-in electrical field established at the interface between $PbSe_2$ and WS_2 to facilitate the separation of photoinduced electron–hole pairs. In explicit, **Figure 5**a shows the I_{ds}–V_{ds} curves of our device with and without light illumination at 635 nm under a zero gate bias. The device gives the obvious photosensitive characteristics with increasing I_{ds} for the increasing light power density from zero to 63.66 mW cm^{-2}. Empirically, the relationship between photocurrent and power density (Φ) follows the equation of

$$I_p = A\Phi^{\alpha} \tag{2}$$

where $I_p = I_{illumination} - I_{dark}$,[4] $I_{illumination}$ is the output current under light illumination, I_{dark} is the output current in the dark state, A and α are fitting parameters. By fitting the extracted data, α is found to be 0.76 for the vdW $PdSe_2/WS_2$ heterostructure photodetector (Figure 5b). This sublinear relationship between I_p and Φ is generally ascribed to complex activities of photo-generated carriers during generation, trapping, and recombination process. On the other hand, responsivity (R) is another figure of merit to evaluate the sensitivity of photodetectors, which is defined as

$$R = I_p/\Phi S \tag{3}$$

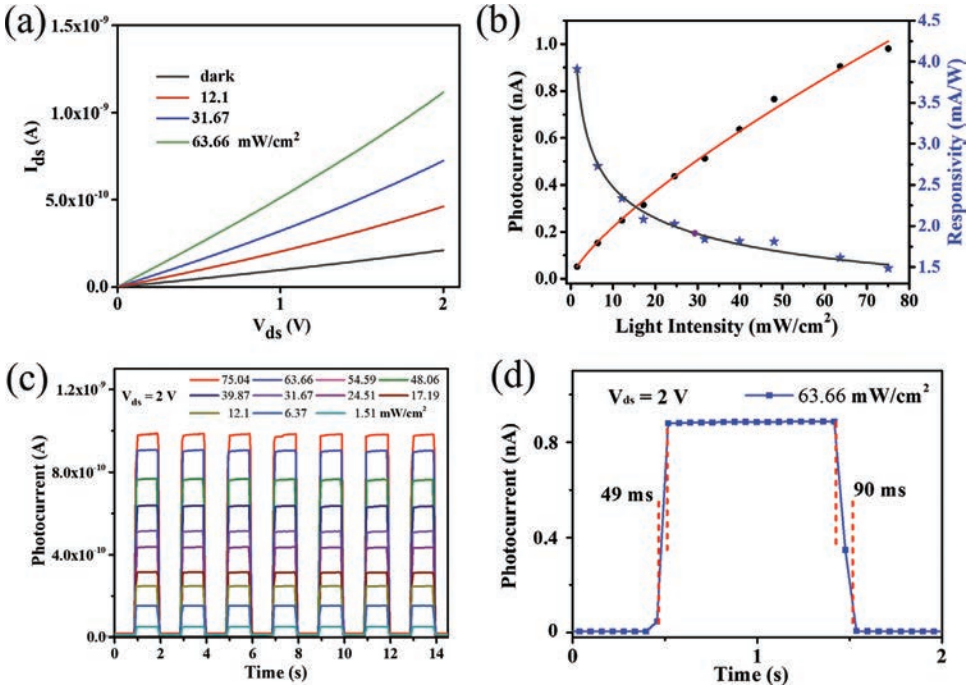

Figure 5. Photoresponse properties of the vdW $PdSe_2/WS_2$ heterostructure photodetector towards 635 nm excitation. a) Photocurrent versus V_{ds} curves under illumination of different light power density. b) Photocurrent and responsivity versus power density. c) Photoresponse under different power density. d) High-resolution photocurrent versus time curve.

where S is the sensitive area of the photodetector, being 440 μm^2 for our devices. It is found that the calculated responsivity can reach up to 3.91 mA W^{-1} at Φ = 1.51 mW cm^{-2} and V_{ds} = 2 V (Figure 5b), which is comparable to those of reported WS_2 and vdW heterostructure-based photodetectors.[12a,27] Also, the calculated R values decrease with the increasing incident light power density that is consistent with cases of WS_2 and vdW heterostructure photodetectors.[20,27b,28] Technically, this high responsivity is believed to arise from defects and charge traps existed at the interface of $PdSe_2/WS_2$. The existence of traps can reduce the recombination rate of holes and electrons, leading to the longer life time, τ, of charge carriers at the relatively low power density. Furthermore, the photogain,

$$G = \tau / t_{trans} \quad (4)$$

(t_{trans} is the transit time of carriers), would increase when the light power density is decreased. In this case, as the light power density increases, high density of photo-excited carriers would fill all trap states, inducing the increase of carrier recombination and thus reducing the responsivity.[12a] Once the incident power density increases, the responsivity gradually gets close to the saturation value of 1.50 mA W^{-1}. Besides the studies of photoresponsivity, Figure 5c as well presents the on–off switching behaviors of the vdW $PdSe_2/WS_2$ heterostructure photodetector under varied power density[13b] at a zero gate bias. The repeatable and reproducible switching on- and off-current confirm the operation stability of the photodetector. Importantly, the response speed of the photodetector can be analyzed accordingly in Figure 5d, where the rise and decay time constants are found as 49 and 90 ms, respectively. In general, the rise (decay) time constant is defined by the time required for the current to increase from 10% to 90% (to decrease from 90% to 10%) of the peak value. In this work, these fast response times are ascribed to the enhanced lifetime of the photogenerated carriers in the heterostructure.

Given that $PdSe_2$ has the higher optical absorbance over a wide spectral range and the narrower band gap than WS_2, we would further investigate the optoelectronic properties of vdW $PdSe_2/WS_2$ heterostructure photodetectors in the infrared regime. Figure S7a, Supporting Information, shows the I_p–V curve under modulation of incident power density of laser at 1550 nm, where the photocurrent increases with the enhancing power density. **Figure 6**a depicts the photocurrent, I_p, and responsivity, R, as a function of light power density, Φ, respectively. The I_p–Φ relationship of the photodetector is then fitted and α is found to be 0.85. The maximum responsivity can reach 0.019 mA W^{-1} while the saturated value would be below 0.015 mA W^{-1}. Also, Figure 6b presents the photo-switching behaviors of the device, demonstrating its good stability and reliability under periodical light illumination (1550 nm). Notably, Figure S7b, Supporting Information, shows its high-resolution photoresponse, in which the rise and decay time constants are found to be 93 and 97 ms, respectively, being comparable to the response times collected at the visible wavelength regime discussed above. We next compile the photoresponse of the vdW heterostructure device under different wavelengths in order to evaluate their broadband photodetection performance. As depicted in Figure 6c, the device shows the photoresponse over a wide spectral range at the same power density with maximum photocurrent observed at 532 nm. The lower photocurrent under 635 nm light irradiation compared with that at 532 nm is mainly attributed to the lower

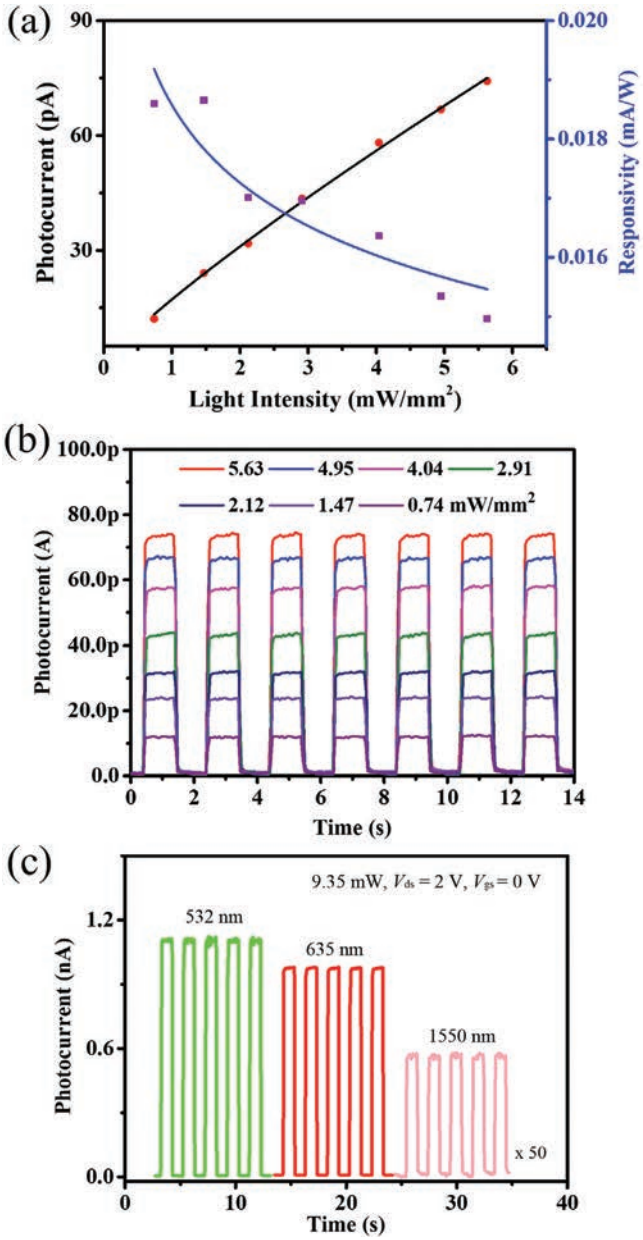

Figure 6. Broadband photoresponse properties of the vdW $PdSe_2/WS_2$ heterostructure photodetector. a) Photocurrent and responsivity versus light power density at 1550 nm. b) Photoresponse under different power density at 1550 nm. c) Photoresponse under different light illumination wavelengths (532, 635, and 1550 nm), at a constant light power of 9.35 mW (light intensity: 74.0 mW cm^{-2}).

light absorption beyond the band edge for the 635 nm light. The type I band alignment of the vdW $PdSe_2/WS_2$ heterostructure is employed to understand the relevant broadband photodetection mechanism (Figure 3c). Under illumination, both intralayer and interlayer excitations are involved to generate electrons and holes in the relevant layers, enabling the fast broadband spectral photoresponse.[4,5b,d,29] On the other hand, photo-excited hole–electron pairs would undergo charge carrier separation in the depletion region, where electrons are transferred into the charge transport layer of WS_2 through the built-in electric filed followed by the relaxation to valance band via interlayer or intralayer transition. This charge separation process has as well been witnessed in other vdW *p–n* heterostructure diodes, where this concept can be inspired to construct devices with *p–n* junctions in order to efficiently enhance the carrier lifetime and the phot ogain.[1b,6c,18a]

3. Conclusion

In conclusion, we have successfully fabricated vdW $PdSe_2/WS_2$ heterostructures through the direct selenization of Pd films on CVD grown monolayer WS_2. The prepared vdW $PdSe_2/WS_2$ heterostructure device displays the *p*-type dominated transport behaviors with on/off current ratio of 10^3 in the ambient condition. Furthermore, the device demonstrates the sensitive and stable photodetection over a wide spectral range from visible to infrared optical communication regions (532–1550 nm). The *p*-$PdSe_2$/*n*-WS_2 junction with built-in electric field is established to realize the efficient charge separation process of photo-excited carriers at the interface of the vdW $PdSe_2/WS_2$ heterostructure, where both intralayer and interlayer excitons are generated and involved in charge transfer allowing for broadband spectral photoresponse. All these findings evidently illustrate the promising potential of constructing vdW heterostructures via simple and direct selenization process for high-performance electronics and optoelectronics.

4. Experimental Section

Synthesis of Monolayer WS_2 Film: A modified process was used based on our previous work.[20] Briefly, a three-zone horizontal tube furnace with a 1 inch diameter quartz tube was employed here. A quartz boat of 200 mg of WO_3 powders was placed in the middle of center zone while a sapphire substrate was positioned at the center of the downstream zone. 300 mg of sulfur powders placed in a ceramic boat was housed in the region right before the carrier gas feeding into the upstream zone, in which these sulfur powders were heated at 160 °C by a heating belt. In order to start the material growth, the pressure was first pumped down to 1 mTorr, then high-purity (99.999%) argon was fed in as a carrier gas at 30 sccm. The pressure was stabilized at 0.16 Torr during the entire growth process. The center zone and the downstream zone were heated to 930 and 910 °C, respectively, whereas the upstream zone was set as idle. The deposition lasted for 40 min. After the deposition was over, the temperature was cooled down to room temperature naturally.

Synthesis of vdW $PdSe_2/WS_2$ Heterostructures: Once the monolayer WS_2 was CVD grown on the sapphire substrate, the entire structure was deposited with Pd films with different controlled thickness at a rate of 0.1 Å s^{-1} (e.g., 0.4 nm for the nominal thickness of Pd). Then, a two-zone furnace with a 1 inch diameter quartz tube was used for the seleniztion of deposited Pd films. In specific, 40 mg of selenium powder placed in a quartz boat was positioned in the center of the upstream zone while sapphire with the Pd/WS_2 structure was placed in the center of downstream zone of the furnace. The upstream and downstream zones were heated to 220 and 420 °C, respectively. The reaction was conducted at a flow rate of 60 sccm of Ar for 60 min, followed by natural cool down to room temperature.

Material Characterizations: An Olympus BX53 optical microscope was used to collect optical microscopy images. An atomic force microscope (diMultiMode V, Veeco) was used to obtain the height profile of fabricated $PdSe_2/WS_2$ heterostructures. The crystallinity of the WS_2 was assessed by using a transmission electron microscope (JEOL 2100F, JEOL Co., Ltd.) after the films were transferred onto the copper grids. Raman mapping image, Raman spectra, and PL spectra were collected

with WITec Alpha 300R using a 532 nm laser. XPS spectra were measured by an X-ray photoelectron spectroscope (ULVAC-PHI5802).

Device Fabrication and Measurement: Photolithography was used to first define the electrode pattern on SiO_2(270 nm)/p^{++}-Si. The successive deposition of Ti (5 nm) and Au (60 nm) was then conducted by e-beam evaporation, followed by a lift-off process. After that, the entire vdW $PdSe_2/WS_2$ heterostructure pre-fabricated on sapphire were subsequently transferred onto the processed SiO_2(270 nm)/p^{++}-Si via polymer-assisted wet-transfer method to complete the device fabrication. Electrical and optoelectronic characterizations of the obtained devices were performed by using a semiconductor analyzer (Agilent B1500A) together with a vacuum probe station. Lasers of 532, 635, and 1550 nm were used as the light excitation source, which was introduced to the device by an optical fiber with a collimator at the end. The power density was measured by a power meter (PM400, Thorlabs). A homemade mechanical chopper controlled by a signal generator was used to modulate the incident light.

Supporting Information

Supporting Information is available from the Wiley Online Library or from the author.

Acknowledgements

X.K. and C.L. contributed equally to this work. This research was financially supported by the General Research Fund (CityU 11204618) and the Theme-based Research (T42-103/16-N) of the Research Grants Council of Hong Kong SAR, China, the Foshan Innovative and Entrepreneurial Research Team Program (NO. 2018IT100031), the National Natural Science Foundation of China (51672229, 61605024, 61775031, 62074024), and Fundamental Research Funds for the Central Universities (ZYGX2018J056) and UESTC Foundation for the Academic Newcomers Award.

Conflict of Interest

The authors declare no conflict of interest.

Data Availability Statement

The data that support the findings of this study are available from the corresponding author upon reasonable request.

Keywords

$PdSe_2/WS_2$, broadband, photodetection, selenization, van der Waals heterostructures

Received: November 18, 2020
Revised: December 17, 2020
Published online: January 20, 2021

[1] a) Q. H. Wang, K. Kalantar-Zadeh, A. Kis, J. N. Coleman, M. S. Strano, *Nat. Nanotechnol.* **2012**, *7*, 699; b) K. F. Mak, J. Shan, *Nat. Photonics* **2016**, *10*, 216; c) D. Lembke, S. Bertolazzi, A. Kis, *Acc. Chem. Res.* **2015**, *48*, 100; d) E. Wu, Y. Xie, J. Zhang, H. Zhang, X. Hu, J. Liu, C. Zhou, D. Zhang, *Sci. Adv.* **2019**, *5*, eaav3430; e) S. Manzeli, D. Ovchinnikov, D. Pasquier, O. V. Yazyev, A. Kis, *Nat. Rev. Mater.* **2017**, *2*, 17033.

[2] a) C. Lan, X. Kang, R. Wei, Y. Meng, S. P. Yip, H. Zhang, J. C. Ho, *ACS Appl. Mater. Interfaces* **2019**, *11*, 35238; b) O. Lopez-Sanchez, D. Lembke, M. Kayci, A. Radenovic, A. Kis, *Nat. Nanotechnol.* **2013**, *8*, 497.

[3] a) M. H. Doan, Y. Jin, S. Adhikari, S. Lee, J. Zhao, S. C. Lim, Y. H. Lee, *ACS Nano* **2017**, *11*, 3832; b) K. Zhang, T. Zhang, G. Cheng, T. Li, S. Wang, W. Wei, X. Zhou, W. Yu, Y. Sun, P. Wang, D. Zhang, C. Zeng, X. Wang, W. Hu, H. J. Fan, G. Shen, X. Chen, X. Duan, K. Chang, N. Dai, *ACS Nano* **2016**, *10*, 3852; c) J. Wang, A. Rousseau, M. Yang, T. Low, S. Francoeur, S. Kena-Cohen, *Nano Lett.* **2020**, *20*, 3651; d) H. Liu, X. Zhu, X. Sun, C. Zhu, W. Huang, X. Zhang, B. Zheng, Z. Zou, Z. Luo, X. Wang, D. Li, A. Pan, *ACS Nano* **2019**, *13*, 13573; e) T. Yang, B. Zheng, Z. Wang, T. Xu, C. Pan, J. Zou, X. Zhang, Z. Qi, H. Liu, Y. Feng, W. Hu, F. Miao, L. Sun, X. Duan, A. Pan, *Nat. Commun.* **2017**, *8*, 1906.

[4] M. Long, Y. Wang, P. Wang, X. Zhou, H. Xia, C. Luo, S. Huang, G. Zhang, H. Yan, Z. Fan, X. Wu, X. Chen, W. Lu, W. Hu, *ACS Nano* **2019**, *13*, 2511.

[5] a) B. Peng, G. Yu, X. Liu, B. Liu, X. Liang, L. Bi, L. Deng, T. C. Sum, K. P. Loh, *2D Mater.* **2016**, *3*, 025020; b) Y. Liu, Z. Gao, Y. Tan, F. Chen, *ACS Nano* **2018**, *12*, 10529; c) M. M. Furchi, A. Pospischil, F. Libisch, J. Burgdorfer, T. Mueller, *Nano Lett.* **2014**, *14*, 4785; d) X. Hong, J. Kim, S. F. Shi, Y. Zhang, C. Jin, Y. Sun, S. Tongay, J. Wu, Y. Zhang, F. Wang, *Nat. Nanotechnol.* **2014**, *9*, 682.

[6] a) H. Xue, Y. Dai, W. Kim, Y. Wang, X. Bai, M. Qi, K. Halonen, H. Lipsanen, Z. Sun, *Nanoscale* **2019**, *11*, 3240; b) Y. Jin, D. H. Keum, S. J. An, J. Kim, H. S. Lee, Y. H. Lee, *Adv. Mater.* **2015**, *27*, 5534; c) F. Wang, Z. Wang, K. Xu, F. Wang, Q. Wang, Y. Huang, L. Yin, J. He, *Nano Lett.* **2015**, *15*, 7558.

[7] Y. Gong, J. Lin, X. Wang, G. Shi, S. Lei, Z. Lin, X. Zou, G. Ye, R. Vajtai, B. I. Yakobson, H. Terrones, M. Terrones, B. K. Tay, J. Lou, S. T. Pantelides, Z. Liu, W. Zhou, P. M. Ajayan, *Nat. Mater.* **2014**, *13*, 1135.

[8] S. J. Haigh, A. Gholinia, R. Jalil, S. Romani, L. Britnell, D. C. Elias, K. S. Novoselov, L. A. Ponomarenko, A. K. Geim, R. Gorbachev, *Nat. Mater.* **2012**, *11*, 764.

[9] R. Cheng, D. Li, H. Zhou, C. Wang, A. Yin, S. Jiang, Y. Liu, Y. Chen, Y. Huang, X. Duan, *Nano Lett.* **2014**, *14*, 5590.

[10] a) S.-Y. Cho, S. J. Kim, Y. Lee, J.-S. Kim, W.-B. Jung, H.-W. Yoo, J. Kim, H.-T. Jung, *ACS Nano* **2015**, *9*, 9314; b) C. Yim, K. Lee, N. McEvoy, M. O'Brien, S. Riazimehr, N. C. Berner, C. P. Cullen, J. Kotakoski, J. C. Meyer, M. C. Lemme, G. S. Duesberg, *ACS Nano* **2016**, *10*, 9550; c) D. Kong, H. Wang, J. J. Cha, M. Pasta, K. J. Koski, J. Yao, Y. Cui, *Nano Lett.* **2013**, *13*, 1341; d) D. Wu, J. Guo, J. Du, C. Xia, L. Zeng, Y. Tian, Z. Shi, Y. Tian, X. J. Li, Y. H. Tsang, J. Jie, *ACS Nano* **2019**, *13*, 9907; e) L. H. Zeng, Q. M. Chen, Z. X. Zhang, D. Wu, H. Yuan, Y. Y. Li, W. Qarony, S. P. Lau, L. B. Luo, Y. H. Tsang, *Adv. Sci.* **2019**, *6*, 1901134.

[11] a) Y. Gao, Z. Liu, D.-M. Sun, L. Huang, L.-P. Ma, L.-C. Yin, T. Ma, Z. Zhang, X.-L. Ma, L.-M. Peng, H.-M. Cheng, W. Ren, *Nat. Commun.* **2015**, *6*, 8569; b) C. Lan, C. Li, J. C. Ho, Y. Liu, *Adv. Electron. Mater.* **2020**, https://doi.org/10.1002/aelm.202000688; c) H. R. Gutierrez, N. Perea-Lopez, A. L. Elias, A. Berkdemir, B. Wang, R. Lv, F. Lopez-Urias, V. H. Crespi, H. Terrones, M. Terrones, *Nano Lett.*. **2013**, *13*, 3447.

[12] a) C. Lan, D. Li, Z. Zhou, S. P. Yip, H. Zhang, L. Shu, R. Wei, R. Dong, J. C. Ho, *Small Methods* **2019**, *3*, 1800245; b) T. Yang, X. Wang, B. Zheng, Z. Qi, C. Ma, Y. Fu, Y. Fu, M. P. Hautzinger, Y. Jiang, Z. Li, P. Fan, F. Li, W. Zheng, Z. Luo, J. Liu, B. Yang, S. Chen, D. Li, L. Zhang, S. Jin, A. Pan, *ACS Nano* **2019**, *13*, 7996; c) C. Ma, Y. Shi, W. Hu, M. H. Chiu, Z. Liu, A. Bera, F. Li, H. Wang, L. J. Li, T. Wu, *Adv. Mater.* **2016**, *28*, 3683.

[13] a) W. Xu, J. Jiang, H. Ma, Z. Zhang, J. Li, B. Zhao, R. Wu, X. Yang, H. Zhang, B. Li, W. Shu, Z. Zhang, B. Li, Y. Liu, L. Liao, X. Duan, *Nano Res.* **2020**, *13*, 2091; b) Q. Liang, Q. Wang, Q. Zhang, J. Wei, S. X. Lim, R. Zhu, J. Hu, W. Wei, C. Lee, C. Sow, W. Zhang, A. T. S. Wee, *Adv. Mater.* **2019**, *31*, e1807609.

[14] L. S. Lu, G. H. Chen, H. Y. Cheng, C. P. Chuu, K. C. Lu, C. H. Chen, M. Y. Lu, T. H. Chuang, D. H. Wei, W. C. Chueh, W. B. Jian, M. Y. Li, Y. M. Chang, L. J. Li, W. H. Chang, *ACS Nano* **2020**, *14*, 4963.

[15] a) T. S. Walmsley, K. Andrews, T. Wang, A. Haglund, U. Rijal, A. Bowman, D. Mandrus, Z. Zhou, Y. Q. Xu, *Nanoscale* **2019**, *11*, 14410; b) W. L. Chow, P. Yu, F. Liu, J. Hong, X. Wang, Q. Zeng, C. H. Hsu, C. Zhu, J. Zhou, X. Wang, J. Xia, J. Yan, Y. Chen, D. Wu, T. Yu, Z. Shen, H. Lin, C. Jin, B. K. Tay, Z. Liu, *Adv. Mater.* **2017**, *29*, 1602969.

[16] A. M. Afzal, G. Dastgeer, M. Z. Iqbal, P. Gautam, M. M. Faisal, *ACS Appl. Mater. Interfaces* **2020**, *12*, 19625.

[17] A. M. Afzal, M. Z. Iqbal, S. Mumtaz, I. Akhtar, *J. Mater. Chem. C* **2020**, *8*, 4743.

[18] a) G. H. Shin, C. Park, K. J. Lee, H. J. Jin, S. Y. Choi, *Nano Lett.* **2020**, *20*, 5741; b) E. Wu, Y. Xie, Q. Liu, X. Hu, J. Liu, D. Zhang, C. Zhou, *ACS Nano* **2019**, *13*, 5430; c) J. Lu, A. Carvalho, H. Liu, S. X. Lim, A. H. Castro Neto, C. H. Sow, *Angew. Chem., Int. Ed.* **2016**, *55*, 11945; d) B. Kang, Y. Kim, W. J. Yoo, C. Lee, *Small* **2018**, *14*, e1802593.

[19] Y. Shao, Y. Liu, X. Chen, C. Chen, I. Sarpkaya, Z. Chen, Y. Fang, J. Kong, K. Watanabe, T. Taniguchi, A. Taylor, J. Huang, F. Xia, *Nano Lett.* **2017**, *17*, 7330.

[20] C. Lan, Z. Zhou, Z. Zhou, C. Li, L. Shu, L. Shen, D. Li, R. Dong, S. P. Yip, J. C. Ho, *Nano Res.* **2018**, *11*, 3371.

[21] a) J. C. Kotsakidis, Q. Zhang, A. L. Vazquez de Parga, M. Currie, K. Helmerson, D. K. Gaskill, M. S. Fuhrer, *Nano Lett.* **2019**, *19*, 5205; b) J. Gao, B. Li, J. Tan, P. Chow, T. M. Lu, N. Koratkar, *ACS Nano* **2016**, *10*, 2628.

[22] a) Y. C. Lin, C. Liu, Y. Yu, E. Zarkadoula, M. Yoon, A. A. Puretzky, L. Liang, X. Kong, Y. Gu, A. Strasser, H. M. Meyer, 3rd, M. Lorenz, M. F. Chisholm, I. N. Ivanov, C. M. Rouleau, G. Duscher, K. Xiao, D. B. Geohegan, *ACS Nano* **2020**, *14*, 3896; b) X. Wu, H. Li, H. Liu, X. Zhuang, X. Wang, X. Fan, X. Duan, X. Zhu, Q. Zhang, A. J. Meixner, X. Duan, A. Pan, *Nanoscale* **2017**, *9*, 4707.

[23] a) B. Zhu, X. Chen, X. Cui, *Sci. Rep.* **2015**, *5*, 9218; b) T. Mueller, E. Malic, *npj 2D Mater. Appl.* **2018**, *2*, 29; c) T. C. Berkelbach, D. R. Reichman, *Annu. Rev. Condens. Matter Phys.* **2018**, *9*, 379.

[24] X. Li, M.-W. Lin, J. Lin, B. Huang, A. A. Puretzky, C. Ma, K. Wang, W. Zhou, S. T. Pantelides, M. Chi, I. Kravchenko, J. Fowlkes, C. M. Rouleau, D. B. Geohegan, K. Xiao, *Sci. Adv.* **2016**, *2*, e1501882.

[25] J. Shang, X. Shen, C. Cong, N. Peimyoo, B. Cao, M. Eginligil, T. Yu, *ACS Nano* **2015**, *9*, 647.

[26] a) C. Lan, X. Kang, Y. Meng, R. Wei, X. Bu, S. P. Yip, J. C. Ho, *Nano Res.* **2020**, *13*, 3278; b) B. Radisavljevic, A. Kis, *Nat. Mater.* **2013**, *12*, 815; c) G. Zhang, M. Amani, A. Chaturvedi, C. Tan, J. Bullock, X. Song, H. Kim, D.-H. Lien, M. C. Scott, H. Zhang, A. Javey, *Appl. Phys. Lett.* **2019**, *114*, 253102.

[27] a) C. Lan, C. Li, Y. Yin, Y. Liu, *Nanoscale* **2015**, *7*, 5974; b) W. Wu, Q. Zhang, X. Zhou, L. Li, J. Su, F. Wang, T. Zhai, *Nano Energy* **2018**, *51*, 45.

[28] G. Sun, B. Li, J. Li, Z. Zhang, H. Ma, P. Chen, B. Zhao, R. Wu, W. Dang, X. Yang, X. Tang, C. Dai, Z. Huang, Y. Liu, X. Duan, X. Duan, *Nano Res.* **2019**, *12*, 1139.

[29] a) P. Rivera, J. R. Schaibley, A. M. Jones, J. S. Ross, S. Wu, G. Aivazian, P. Klement, K. Seyler, G. Clark, N. J. Ghimire, J. Yan, D. G. Mandrus, W. Yao, X. Xu, *Nat. Commun.* **2015**, *6*, 6242; b) L. Wang, M. Tahir, H. Chen, J. B. Sambur, *Nano Lett.* **2019**, *19*, 9084.